

Maximum-Likelihood-Based Position Decoding of Laser-Processed Converging-Pixel CsI: Tl Detectors for High-Resolution SPECT

Xi Zhang, Arkadiusz Sitek, Lisa Blackberg, Matthew Kupinski, Lars Furenlid, Hamid Sabet

Abstract—This study demonstrates the feasibility of a novel fabrication technique for high-spatial-resolution CsI: Tl scintillation detectors tailored for single-photon emission computed tomography (SPECT) systems. Building upon our previously developed laser-induced optical barrier (LIOB) method—which achieved high spatial resolution, excellent sensitivity, and 100% fabrication yield in CsI: Tl detectors—we extend this approach to a converging-pixel architecture. A CsI: Tl crystal array with converging pixels was designed and fabricated, featuring entrance-face pixels of $1.6 \times 1.6 \text{ mm}^2$ and photodetector-side pixels of $2 \times 2 \text{ mm}^2$. To localize γ -ray interactions, both the center-of-gravity (CoG) algorithm and a maximum-likelihood (ML)-based decoding method were implemented. A custom-built four-axis motion platform was developed to deliver a finely collimated pencil beam at precisely controlled positions and angles across the array, enabling generation of a comprehensive dataset for prior knowledge and validation. The results demonstrate an energy resolution of $11.79 \pm 0.53\%$ (collimated experiment) and a position localization accuracy of $1.00 \pm 0.42 \text{ mm}$ (nearest-neighbor interpolation), confirming that the proposed converging-pixel architecture, combined with statistical decoding algorithms, provides a promising path toward the development of high-performance SPECT detectors.

Index Terms—Converging pixels, CsI: Tl crystal, laser induced optical barrier, maximum likelihood-based algorithm, SPECT

I. INTRODUCTION

SINGLE photon emission computed tomography (SPECT) is an established nuclear medicine modality capable of capturing functional and physiological information essential for accurate disease diagnosis and therapeutic planning. Clinically, SPECT is widely used for brain function evaluation, skeletal imaging, and myocardial perfusion assessment[1-4]. Despite its diagnostic value, SPECT imaging suffers from inherent limitations, particularly in spatial resolution, which remains lower than that of positron

This work was supported in part by NIH Grant No. R01HL145160 and R01EB034785.

X Zhang, A Sitek, H Sabet {xzhang84, asitek, hsabet}@mgh.harvard.edu are with Department of Radiology, Massachusetts General Hospital, Harvard Medical School, Boston, MA, 02129, US.

L. Furenlid, M. Kupinski. arizona.edu are with University of Arizona, Tucson, AZ 85721, US.

L. Blackberg was with the Department of Radiology, Massachusetts General Hospital, Harvard Medical School, Boston, MA, 02129, US.

emission tomography (PET). This limitation hinders the accurate delineation of small lesions and consequently affects the precision of both diagnostic imaging and radionuclide therapy[5-7]. Current clinical SPECT systems typically achieve an energy resolution of approximately 10% at 140 keV and an intrinsic spatial resolution below 5 mm[8]. As the extrinsic resolution is primarily governed by the collimator geometry (typically 6–15 mm at a 10 cm distance)[9], substantial research efforts in both hardware and software development have been undertaken to emphasize high-performance detector design and dedicated scan sampling schemes, which eventually lead to improvement on the spatial resolution and sensitivity of SPECT[10-12].

As the primary determinant of SPECT performance, detector development has focused on optimizing scintillator materials and structures, electronic readout, and pinhole collimator design. In terms of scintillator materials, halide crystals such as CsI: Tl and NaI: Tl have been widely employed due to their high light yield. More recently, LYSO and GAGG crystals have gained attention for their higher density and effective atomic number [13]. Semiconductor materials such as cadmium zinc telluride (CZT) also provide excellent energy and spatial resolutions, making them a major focus of research[14-16]. However, their incomplete charge collection and high production cost have limited their widespread adoption in SPECT applications. Traditionally, scintillator arrays are fabricated through mechanical pixelation, in which a bulk crystal is sequentially cut, polished, and separated by reflective materials to form discrete pixels. Although this technique allows for position decoding, it becomes increasingly labor-intensive and expensive as pixel sizes shrink below the millimeter scale.[17, 18]. Furthermore, the inclusion of reflectors reduces the packing fraction and decreases detection sensitivity. In contrast, continuous scintillator crystals overcome these manufacturing limitations by eliminating dead space introduced by reflectors, thereby providing higher sensitivity, improved packing efficiency, and enhanced detection performance [19-21]. For the readout electronics, silicon photomultipliers (SiPMs), also known as multi-pixel photon counters (MPPCs), have increasingly replaced traditional photomultiplier tubes (PMTs) in nuclear medicine imaging owing to their high gain, compact size, compatibility with magnetic fields, and low operating voltage. In addition, application-specific integrated circuits (ASICs) have been developed as alternatives to conventional analog

readout architectures. These integrated solutions are designed for dedicated tasks such as individual SiPM readout in PET systems and typically incorporate preamplification, timing, pulse-shaping, and sample-and-hold functionalities[22-24].

However, accurately decoding the interaction position of γ -photons in continuous scintillator crystals remains a major challenge. Positioning algorithms for such detectors can generally be classified into three categories: non-calibration methods based on light-distribution characteristics, statistical approaches relying on calibration data, and machine learning methods [25]. Among these, the center-of-gravity (CoG) algorithm is the simplest and most direct light-profile-based method, offering fast computation without requiring calibration data. However, it suffers from limited positioning accuracy and pronounced edge effects [26-28]. Statistical approaches, such as the Least Squares, Nearest Neighbor, and Maximum Likelihood (ML) methods, employ pre-calibrated datasets—either experimentally measured or theoretically simulated—to model the photodetector response as a function of interaction position [29-32]. These methods aim to improve spatial resolution and expand the effective volume of monolithic scintillator detectors. Their primary limitation, however, lies in the dependence on accurate calibration data. Among them, the ML approach allows the incorporation of prior information and has been demonstrated to achieve superior spatial resolution. In recent years, artificial intelligence (AI) techniques have been increasingly applied in medical imaging and radiation therapy evaluation[33-36]. Although the high computational cost once constrained the application of neural networks in continuous-crystal decoding, the widespread availability of GPU-based computing has progressively mitigated this limitation, enabling the development of data-driven positioning algorithms with improved efficiency and scalability.

Conventional SPECT systems typically employ either parallel-hole or pinhole collimators. Parallel-hole collimators are widely used but suffer from limited sensitivity and spatial resolution, whereas pinhole collimators provide geometric magnification at the expense of sensitivity and field of view[37, 38]. In contrast, detectors incorporating converging pixels—such as inward-converging geometries—can simultaneously enhance spatial resolution and sensitivity while maintaining image magnification [39-41]. This configuration can also reduce acquisition time and/or administered dose without compromising reconstructed image resolution compared with conventional low-energy high-resolution (LEHR) collimators. Furthermore, by integrating attenuation, scatter, and motion corrections, converging-pixel detectors can minimize statistical uncertainties and reduce image artifacts or misregistration, thereby improving image alignment and overall quantitative accuracy.

Given the reliability and precision of laser systems, laser-based techniques for scintillator pixelation have attracted increasing attention. In our previous work, the laser-induced optical barrier (LIOB) approach utilized tightly focused, high-intensity laser pulses to introduce localized modifications

within the scintillator bulk [42]. Due to the low thermal conductivity of the crystal, these laser interactions generate microstructures with altered refractive indices. By accurately controlling the laser energy, pulse duration, and focusing conditions, well-defined pixel-like patterns can be inscribed without mechanical segmentation, enabling the fabrication of fine-pitch CsI: Tl scintillator arrays with 100% process yield and improved spatial resolution and detection sensitivity. Building upon this foundation, the present study extends the LIOB technique to a converging-pixel CsI: Tl crystal specifically designed for SPECT applications. The custom-fabricated array features entrance-face pixels measuring $1.6 \times 1.6 \text{ mm}^2$ that expand to $2 \times 2 \text{ mm}^2$ at the photodetector interface, guiding scintillation light toward the photosensors and enhancing photon collection efficiency. A precision four-axis motion platform was developed to deliver finely collimated pencil-beam radiation for algorithm calibration and validation. The resulting decoding maps were subsequently analyzed to evaluate the performance of the event positioning algorithms.

II. MATERIALS AND METHODS

A. LIOB CsI: Tl Crystal

The concept of LIOB technique is illustrated in Fig. 1(a) and described in detail in[42]. Using this method, a CsI: Tl scintillator with dimensions of $50 \times 50 \times 8.05 \text{ mm}^3$ was laser-processed into a 25×25 pixel array, corresponding to a pixel pitch of 2 mm at the photodetector plane and 1.6 mm at the entrance plane. Four layers of Teflon tape were wrapped around five faces of the crystal, excluding the light-output surface, to provide diffuse reflection. A 1.5-mm-thick light guide was optically coupled to the array using optical adhesive (DOWSIL Q2-3067) to ensure efficient optical transmission.

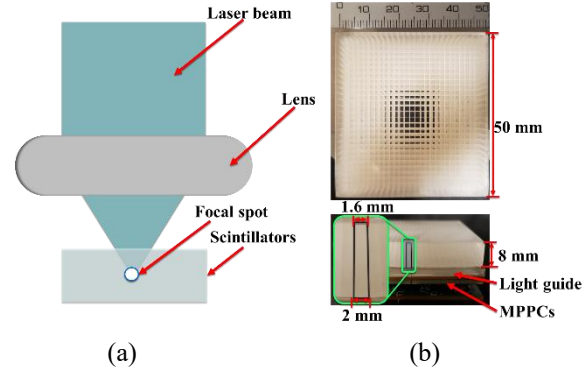


Fig. 1. (a) Schematic illustration of the laser-induced optical barrier process; (b) photograph of the fabricated CsI: Tl crystal array.

B. Readout electronics

The readout system consisted of an 8×8 multipixel photon counter (MPPC) array, a self-designed 64-channel analog front-end board, two flexible printed cables (FPCs), and a CAEN V1740 waveform digitizer. The MPPC array (model S14161-3050AS-08, Hamamatsu Photonics) comprises 64 individual pixels with a $50 \mu\text{m}$ microcell pitch and a total of

> REPLACE THIS LINE WITH YOUR MANUSCRIPT ID NUMBER (DOUBLE-CLICK HERE TO EDIT) <

3531 microcells per pixel. The effective photosensitive area measures $25.8 \times 25.8 \text{ mm}^2$, with 0.2 mm edge gaps between the active region and the package boundary. The 64-channel analog board was designed to amplify and condition the energy signals read from the MPPC array. The processed signals were then transmitted through FPCs to the CAEN V1740 digitizer for waveform acquisition. The V1740 module features a 12-bit flash ADC with a 62.5 MS/s sampling rate, suitable for mid-speed signals from inorganic scintillators coupled to MPPCs. The MPPC array was biased at 41 V using a CAEN DT5485 high-voltage power supply.

C. Experimental setting

To generate robust training datasets for maximum-likelihood positioning, a custom four-axis motion collimation platform was developed. The system enabled precise bidirectional translation along the X and Y axes and rotational adjustment about the φ and θ angles to ensure accurate beam alignment. A tungsten collimator, designed to accommodate a capillary tube, was fabricated with a 1-mm-diameter aperture to produce a fine pencil beam. The capillary was filled with a ^{99m}Tc solution at an activity concentration of $185 \text{ MBq}\cdot\text{cm}^{-3}$. Data were acquired over a 25×25 grid of collimation positions, with each position irradiated for 15 s, yielding 625 discrete datasets for algorithm training and validation. The entire experiment was completed within approximately 3 h—corresponding to half the half-life of ^{99m}Tc —to minimize the effect of radioactive decay on the measured activity.

For performance evaluation, a flood irradiation experiment was conducted using a ^{57}Co point-like source with an activity of 15.4 kBq. The acquisition time was 1200 s, during which 962,990 total counts were recorded.

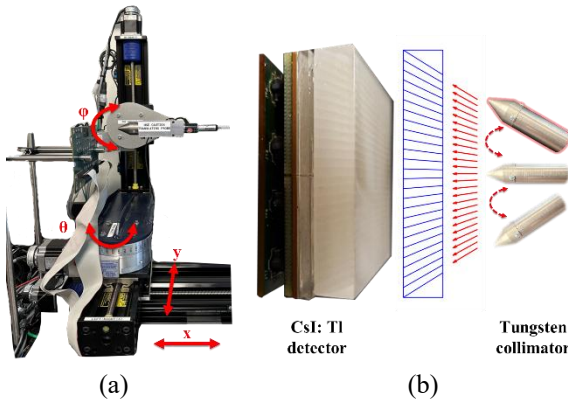


Fig. 2. (a) Collimation system based on a four-axis motion platform; (b) CsI: Tl detector, tungsten collimator, and calibration schematic diagram.

D. Position decoding algorithm

1) Center of Gravity

The CoG method is one of the most widely used non-calibration approaches that estimate interaction positions based on the spatial distribution of scintillation light. In this study, the photon interaction positions were determined using the CoG algorithm, as described below.

$$\begin{cases} x = \frac{P}{8} * \left(\frac{E_{r,1}+2*E_{r,2}+3*E_{r,3}+\dots+7*E_{r,7}+8*E_{r,8}}{E_{total}} - 1 \right) \\ y = \frac{P}{8} * \left(\frac{E_{c,1}+2*E_{c,2}+3*E_{c,3}+\dots+7*E_{c,7}+8*E_{c,8}}{E_{total}} - 1 \right) \end{cases} \quad (1)$$

where x and y denote the calculated interaction coordinates on a flood map of $P \times P$ pixels. $E_{r,n}$ represents the energy signals measured from the n_{th} row of MPPCs. $E_{c,n}$ represents the energy signals measured from the n_{th} column of MPPCs. E_{total} denotes the total energy summed over all 64 MPPC channels.

Noise suppression method: The overall electronic noise—originating from MPPC dark current and the readout circuitry—can significantly degrade the quality of the crystal flood map. In our previous work, two simple noise-suppression strategies were introduced[43]. In this study, we employed a different approach: for each event, the 64-channel energy signals were processed by subtracting the n_{th} largest signal (N_{th}) in each event. Negative results were set to zero, while positive values were retained as the residual differences.

$$S_{out,i} = \begin{cases} S_{in,i} - N_{th} & \text{if } S_{in,i} > N_{th} \\ 0 & \text{if } S_{in,i} \leq N_{th} \end{cases} \quad (2)$$

2) Maximum likelihood

A statistical approach based on the ML method can, to some extent, mitigate the impact of various types of noise on decoding by utilizing prior data. This method is particularly effective near the crystal edges, where it often outperforms conventional analytical techniques. For the case in which a γ -ray deposits energy E in pixel i , the log-likelihood associated with the measured charge distribution $\mathbf{q} = \{q_j\}$ can be expressed as:

$$\mathcal{L}_i(i, E^{(n)} | \mathbf{q}) = \sum_j q_j \log[c_{i,j}E] - c_{i,j}E \quad (3)$$

where q_j denotes the signal collected by the MPPC labeled j , and \mathbf{q} represents the set of all measured charges. The coefficient $c_{i,j}$ corresponds to the fraction of scintillation photons expected to be detected by MPPC j when the scintillation event originates from pixel i , which is also called mean detector response function (MDRF). For each pixel position, 6,000 events within an energy window of 20% were employed to calibrate and obtain $c_{i,j}$.

The crystal pixel $i^{(n)}$ most likely to have absorbed the γ -ray is determined by the index that maximizes the log-likelihood function:

$$i^{(n)} = \underset{i}{\operatorname{argmax}} \mathcal{L}_i(i, E^{(n)} | \mathbf{q}) \quad (4)$$

where the superscript (n) refers to the iteration number. Likewise, $E^{(n)}$ denotes the energy estimate after the n_{th} update. This result can be employed to refine the energy estimate after the pixel with the highest likelihood is identified.

$$E^{(n+1)} = \frac{\sum_j q_j}{\sum_j c_{i^{(n)},j}^{(n)}} \quad (5)$$

In practice, the MDRF is typically sampled on a coarse spatial grid and then interpolated to obtain values on a finer grid. In this study, three interpolation schemes—bilinear, bicubic, and nearest-neighbor—were applied to the MDRF. Because the interpolated likelihood values are often very similar, even small variations can shift the decoded event position by one pixel. The subsequent results indicate that the

> REPLACE THIS LINE WITH YOUR MANUSCRIPT ID NUMBER (DOUBLE-CLICK HERE TO EDIT) <

choice of interpolation method has a measurable influence on the overall decoding performance.

E. Assessment of the decoding map

Peak to valley ratio: The peak-to-valley ratio (PVR) is one of the primary metrics used to assess the decoding performance of PET and SPECT detectors. For the collimated dataset, a total of $6000 \times 25 \times 25$ events were aggregated, decoded based on the MDRF, and used to generate histograms for PVR evaluation. For the flood-irradiation dataset, the flood maps were directly decoded using the ML algorithm, followed by PVR analysis.

Segmentation and position error: To quantify the decoding accuracy, regional segmentation of the decoded maps was performed. Different interpolation methods employed distinct segmentation strategies. After segmenting the flood maps, decoding errors were evaluated using collimated data along selected columns. The analysis included (1) intensity profile inspection to visualize the separation of adjacent crystals. (2) positional error quantification, in which the pixel center was taken as the reference position and the deviation between the decoded and true collimated positions was measured. The same procedure was applied to all positions to obtain the overall error distribution.

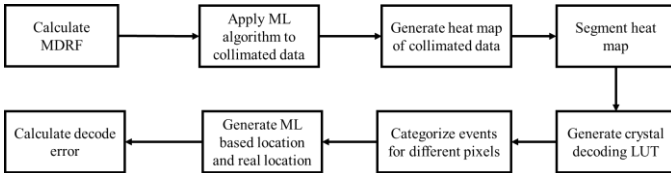


Fig. 3. Workflow of decoding error calculation

III. RESULTS

A. Energy resolution

The energy resolution measured from the flood irradiation experiment was 15.76%, and the corresponding energy spectrum is shown in Fig. 4(a). From the collimated measurements acquired at 625 positions, individual energy spectra were obtained, yielding an average energy resolution of $11.79 \pm 0.53\%$. The spectra corresponding to the pixel located at the first row and first column, and the central pixel (highlighted in red in Fig. 4(b)) are shown in Fig. 4(c) and Fig. 4(d), respectively.

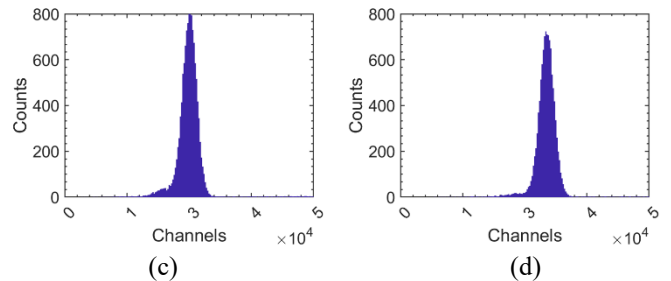
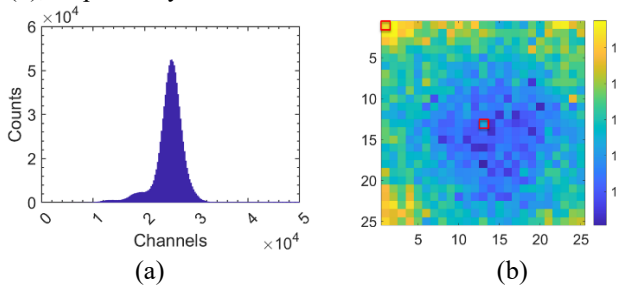


Fig. 4. (a) Energy spectrum obtained from the flood irradiation experiment; (b) energy resolution map derived from the calibrated 625 collimation positions, with two selected crystal pixels marked by red squares; (c) energy spectrum from the pixel located at the first row and first column; and (d) energy spectrum from the central pixel.

B. CoG Results

1) Flood irradiation data

The CoG method was applied to decode the flood irradiation data within an energy window of 20%, and the corresponding results are shown in Fig. 5. Figures 5(a) and 5(b) present the decoding maps obtained with and without the noise-suppression method, respectively. Parameter n in equation (2) was optimized and set to 16. Figures 5(c) and 5(d) show the horizontal profiles along the x -direction. The peak-to-valley ratio at the central column was 1.91, and approximately 15 \times 15 pixels in the central region could be clearly identified. However, the pixels at the edges and corners were strongly merged, making them indistinguishable. In addition, the nonuniform distribution of the decoded spots complicated map segmentation for subsequent image reconstruction.

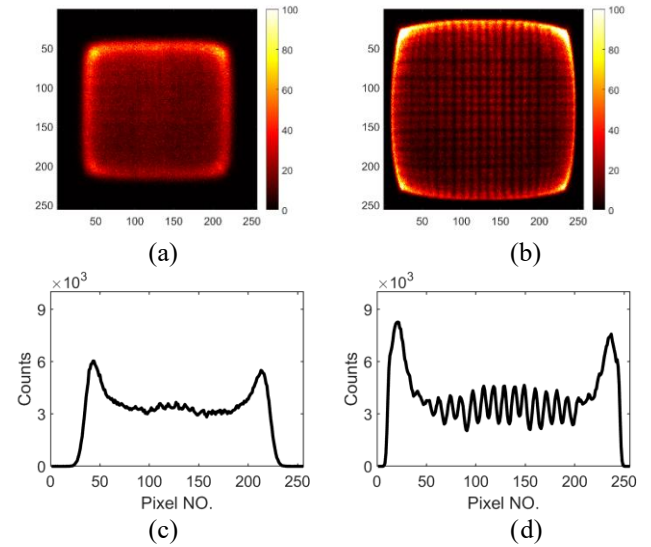


Fig. 5. Decoding maps of the flood irradiation results obtained (a) without and (b) with the noise-suppression technique; event-count profiles (c) without and (d) with noise suppression.

2) Collimated data

A total of 625 datasets were acquired in the collimation experiments. For each collimation position, 6000 events within a 20% energy window were randomly selected and combined to construct the complete collimated dataset. The

> REPLACE THIS LINE WITH YOUR MANUSCRIPT ID NUMBER (DOUBLE-CLICK HERE TO EDIT) <

data quality was preliminarily evaluated using the CoG method. Figure 6 shows the decoding maps and the corresponding profile plots. Because the calibration data covered only a portion of each pixel, the decoded spots in the maps appeared clearer than those from the flood irradiation data. However, overlapping among pixels remained noticeable at the edges and corners. In addition, nonuniform distribution persisted, resulting in only 13 distinguishable peaks and valleys in the profile plot.

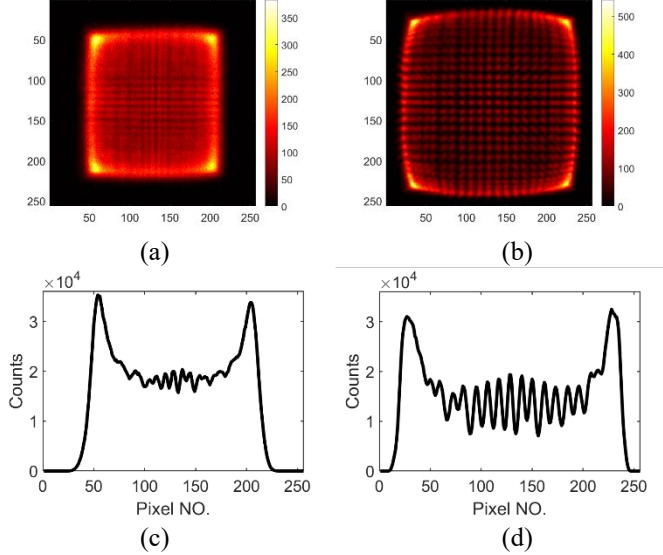


Fig. 6. Decoding maps of the collimated results obtained (a) without and (b) with the noise-suppression technique using the CoG algorithm; event-count profiles (c) without and (d) with noise suppression.

C. ML results

1) Measured MDRF

Based on the datasets from the collimated experiments, the coefficient $c_{i,j}$, representing the fraction of scintillation photons expected to be detected by MPPC j when the scintillation event originates from pixel i , were calculated and shown in Fig. 7 (a). In this study, i corresponds to the 8×8 MPPC channels, and j corresponds to the 25×25 collimation positions. Because the coefficient values were very close to each other, even minor variations in the likelihood could decisively affect the event assignment, occasionally resulting in a one-pixel misplacement. For implementation in the ML algorithm, the coefficient matrix was interpolated from 64×625 to $64 \times (256 \times 256)$ and $64 \times (512 \times 512)$ using linear, bicubic, and nearest-neighbor interpolation methods to compare and optimize decoding performance. Figures 7(b)–7(d) display the interpolated MDRFs with a size of $64 \times (256 \times 256)$, illustrating that the differences among the interpolation methods were minimal.

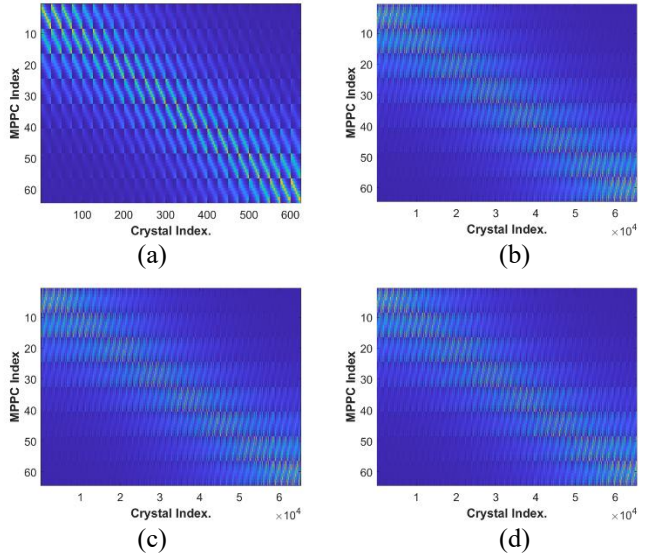
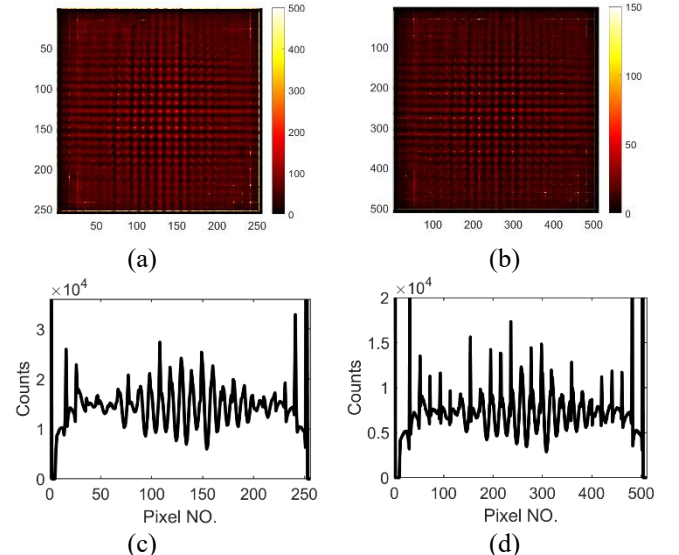


Fig. 7. (a) Scintillation light-response matrix (64×625); interpolated light-response matrices obtained using (b) linear, (c) bicubic, and (d) nearest-neighbor interpolation methods ($64 \times 256 \times 256$).

2) Collimated data

Bilinear method: Fig. 8 shows the decoding maps and count-profile plots obtained from the collimated dataset using bilinear interpolation. The peak-to-valley ratios of the central column were 3.47 and 3.51 for map pixel sizes of 256 and 512, respectively. The decoding maps indicate that the datasets corresponding to different collimation positions were relatively uniformly distributed across the image, without exhibiting the compression typically observed in the CoG decoding maps. However, in the profile plots, only about 13 peaks and valleys were distinguishable, and the decoding map clearly resolved only an approximately 8×8 crystal region. The decoding performance in the edge and corner regions was, to some extent, inferior to that of the CoG method. In addition, a considerable number of artifacts were observed in the decoding maps, including abnormal patterns on the decoded spots and unusually bright regions along the edges.



> REPLACE THIS LINE WITH YOUR MANUSCRIPT ID NUMBER (DOUBLE-CLICK HERE TO EDIT) <

Fig. 8. Decoding maps of the collimated experiments obtained using bilinear interpolation with the ML algorithm at pixel resolutions of (a) 256×256 and (b) 512×512 ; corresponding event-count profiles are shown in (c) and (d), respectively.

Bicubic method: Using the bicubic interpolation method, the decoding maps and event-count profiles of the collimated dataset were obtained, as shown in Fig. 9. The decoding maps demonstrated that this method was able to resolve nearly all 25×25 pixels with a relatively uniform distribution, which is advantageous for subsequent pixel segmentation. Even at the crystal edges and corners, several decoded spots remained clearly distinguishable. The event-count profiles indicated peak-to-valley ratios of 6.09 and 6.47 for pixel resolutions of 256 and 512, respectively. Twenty-five distinct peaks corresponding to the 25 pixel columns were clearly identified in the profiles. Although the edge crystals were successfully decoded, edge effects were still present, resulting in a noticeable decrease in the peak-to-valley ratio near the boundaries.

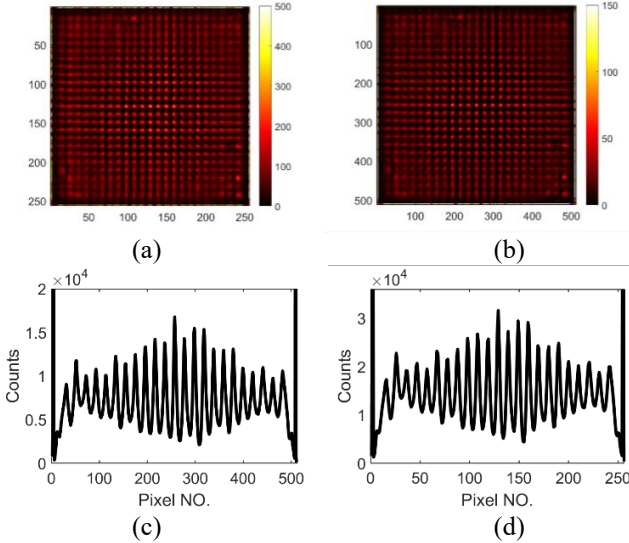


Fig. 9. Decoding maps of the collimated experiments obtained using bicubic interpolation with the ML algorithm at pixel resolutions of (a) 256×256 and (b) 512×512 ; corresponding event-count profiles are shown in (c) and (d), respectively.

Decoding error analysis was subsequently performed for the bicubic interpolation using the ML algorithm. Based on the overall decoding map, the image was segmented into 25×25 regions, and a lookup table was established to determine which crystal pixel each event was decoded to, as shown in Fig. 10(c). The decoded crystal positions were then compared with the actual collimation positions to calculate the positional errors. For detailed evaluation, 25 collimation datasets along the central column were analyzed. Their event-count profiles are shown in Fig. 10(a), where a baseline offset of 1000 was applied to facilitate comparison among the decoding results. The black dashed lines indicate the segmentation boundaries. In the central region, the collimated events were well localized, with only a small fraction misassigned to adjacent pixels. Figure 10(b) shows the decoding errors for the 25 datasets, with the mean absolute error ranging from 0.16 mm at the central pixels to 0.96 mm at the edges. Figure 10(d)

summarizes the decoding errors across all 25×25 pixels, yielding an average value of 1.07 ± 0.45 mm. These results highlight a pronounced edge effect, characterized by higher decoding accuracy in the central region and reduced accuracy at the periphery.

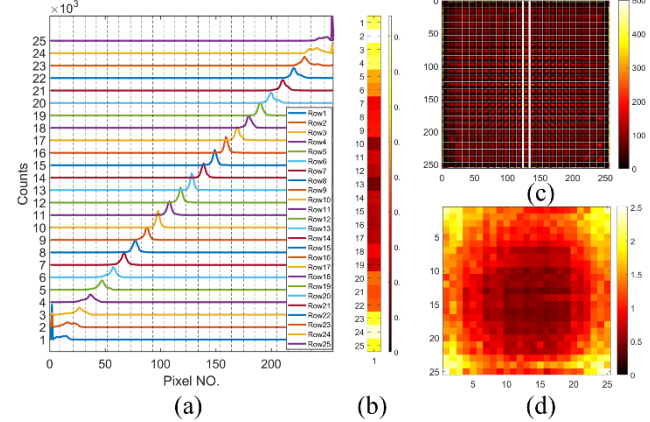


Fig. 10. Bicubic interpolation: (a) event-count profiles of the 25 collimation datasets along the central column, with a baseline offset of 1000 applied to each step; the black dashed lines indicate the image segmentation boundaries; (b) positional errors of the selected datasets; (c) segmented decoding map, where the decoding region corresponding to the selected 25 datasets is highlighted between the two white lines; and (d) positional errors of all 25×25 collimation datasets.

Nearest-neighbor method: Figure 11 shows the decoding results of the collimated dataset obtained using the nearest-neighbor interpolation at pixel resolutions of 256×256 and 512×512 . Unlike the bilinear and bicubic methods, the nearest-neighbor approach produced discrete decoding results. In the decoding maps, all 25×25 decoding positions were clearly identified, and the corresponding event-count profiles exhibited 25 distinct peaks, indicating that the method successfully classified the collimated datasets into 25×25 discrete positions.

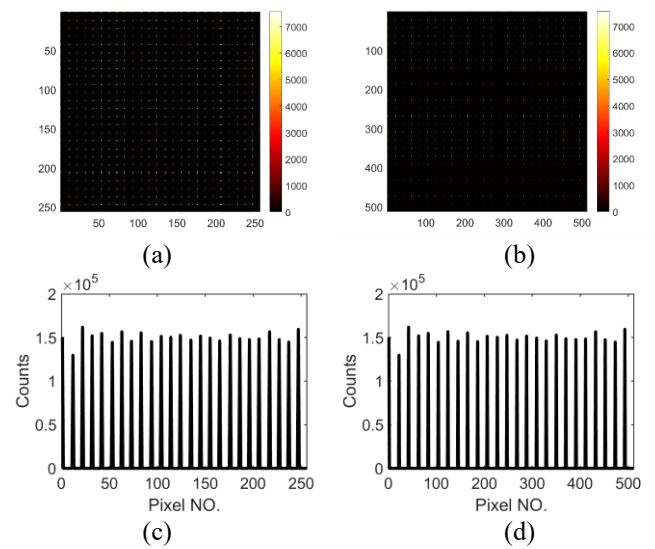


Fig. 11. Decoding maps of the collimated experiments obtained using nearest-neighbor interpolation with the ML

algorithm at pixel resolutions of (a) 256×256 and (b) 512×512 ; corresponding event-count profiles are shown in (c) and (d), respectively.

The nearest-neighbor interpolation method could not be evaluated using peak-to-valley ratio analysis; therefore, its decoding performance was assessed through positional error analysis. Similar to the bicubic interpolation analysis, the overall decoding map was segmented into 25×25 regions, and a lookup table was established, as shown in Fig. 12(c). The discrete decoding points made the segmentation process straightforward and unambiguous. Twenty-five collimation datasets along the central column were analyzed, and their event-count profiles are shown in Fig. 12(a). A baseline offset of 5000 was applied to facilitate comparison among the decoding results. The black dashed lines indicate the image segmentation boundaries. Figure 12(b) presents the decoding errors for the 25 datasets, with the minimum mean absolute error of 0.18 mm observed at the central pixels and the maximum error of 1.01 mm at the edges. Figure 12(d) summarizes the decoding errors across all 25×25 pixels, yielding an average positional error of 1.00 ± 0.42 mm.

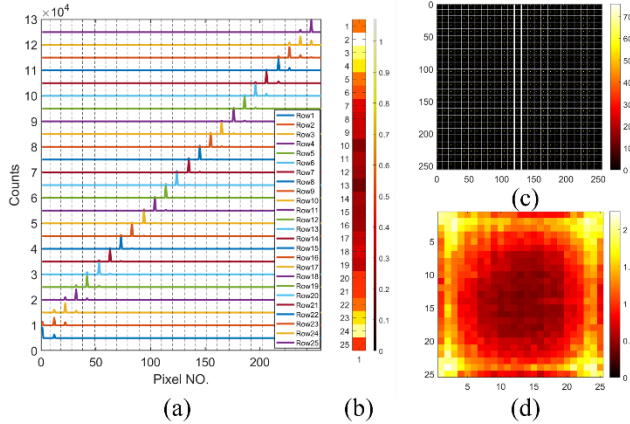


Fig. 12. Nearest-neighbor interpolation: (a) event-count profiles of the 25 collimation datasets along the central column, with a baseline offset of 5000 applied to each step; the black dashed lines indicate the image segmentation boundaries; (b) positional errors of the selected datasets; (c) segmented decoding map, where the decoding region corresponding to the selected 25 datasets is highlighted between the two white lines; and (d) positional errors of all 25 \times 25 collimation datasets.

3) Flood data

Since the ML method demonstrated superior performance with the collimated datasets, its application was further extended to the flood-irradiation data. Figures 13–15 present the decoding results obtained using bilinear, bicubic, and nearest-neighbor interpolation methods, respectively, at pixel resolutions of 256×256 and 512×512 , together with the corresponding event-count profiles along the x -direction. Similar to the collimated results, the bilinear interpolation method exhibited limited discrimination among crystal pixels and introduced noticeable artifacts.

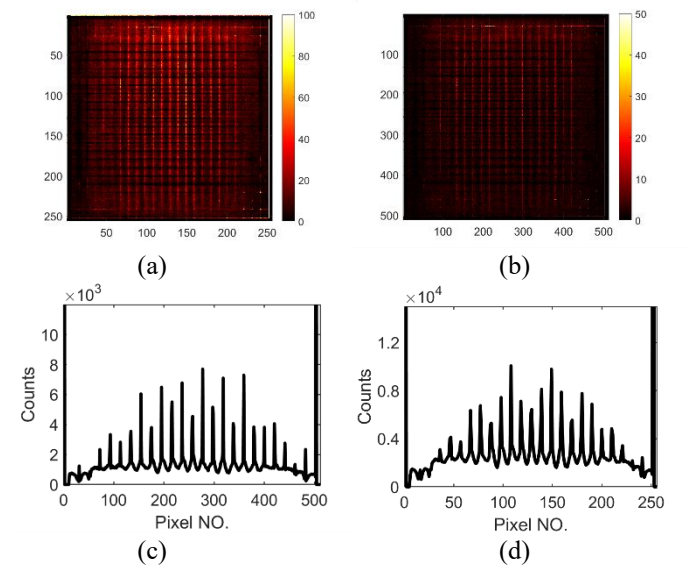
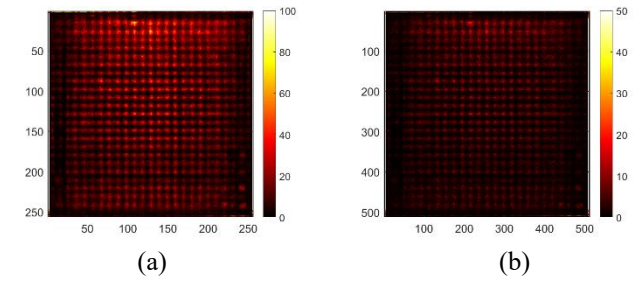


Fig. 13. Decoding maps of the flood-irradiation dataset obtained using bilinear interpolation with the ML algorithm at pixel resolutions of (a) 256×256 and (b) 512×512 ; corresponding event-count profiles are shown in (c) and (d), respectively.

The bicubic interpolation method successfully resolved most of the crystal pixels, with distinct pixel distributions observed even at the edges and corners. The event-count profiles showed that although the decoding performance degraded toward the periphery, 25 peaks corresponding to the 25 rows of crystal pixel positions remained readily distinguishable. The peak-to-valley ratios of the central column reached 2.89 and 3.17 for pixel resolutions of 256×256 and 512×512 , respectively, enabling clear pixel discrimination and thereby improving positioning accuracy when compared with the CoG algorithm.

The nearest-neighbor interpolation approach also achieved discrete decoding of the 25×25 positions. Although its performance could not be evaluated using the peak-to-valley ratio metric, the decoding results from the collimated dataset suggested that its positioning accuracy was slightly superior to that of the bicubic approach, with the added advantage of facilitating straightforward segmentation of the decoding maps.



> REPLACE THIS LINE WITH YOUR MANUSCRIPT ID NUMBER (DOUBLE-CLICK HERE TO EDIT) <

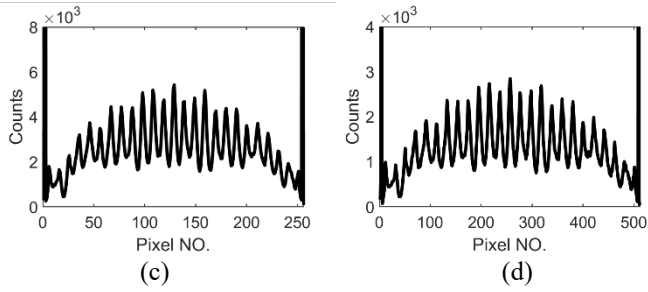


Fig. 14. Decoding maps of the flood-irradiation dataset obtained using bicubic interpolation with the ML algorithm at pixel resolutions of (a) 256×256 and (b) 512×512 ; corresponding event-count profiles are shown in (c) and (d), respectively.

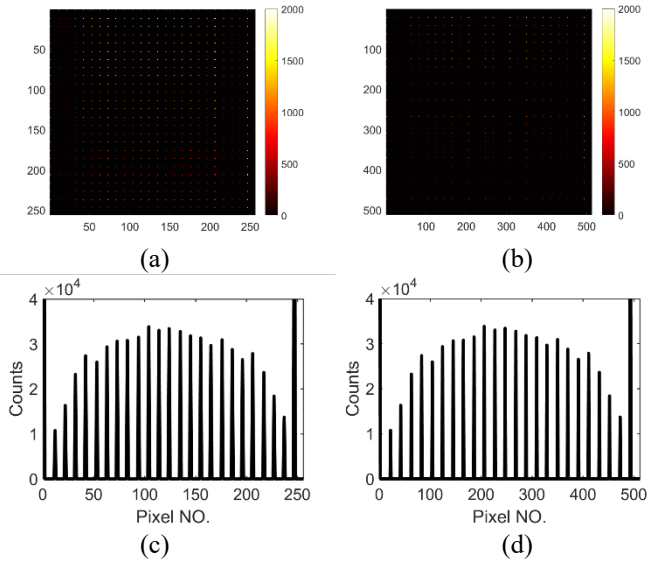


Fig. 15. Decoding maps of the flood-irradiation dataset obtained using nearest-neighbor interpolation with the ML algorithm at pixel resolutions of (a) 256×256 and (b) 512×512 ; corresponding event-count profiles are shown in (c) and (d), respectively.

IV. DISCUSSION AND CONCLUSION

This study implemented a laser-processed optical barrier technique to fabricate converging pixels within a CsI: Tl crystal, aiming to enhance decoding performance while maintaining the inherent advantages of higher sensitivity and improved packing efficiency for SPECT detectors. The fabricated crystal featured converging pixels with a 2 mm pitch at the photodetector plane and a 1.6 mm pitch at the entrance surface. A custom-built four-axis motion platform was developed to enable high-precision calibration of the 25×25 converging pixels at specific incident angles. Both collimated and flood-irradiation datasets were decoded and compared using the CoG and ML methods. For the ML approach, three interpolation schemes—bilinear, bicubic, and nearest-neighbor—were investigated. The CoG method achieved satisfactory decoding performance in the central crystal region (15×15), yielding a peak-to-valley ratio of 1.91. In contrast, the ML method with bicubic interpolation successfully resolved all pixels, producing a peak-to-valley ratio of approximately 3 in the central region, while the

nearest-neighbor approach achieved similarly complete decoding. The bilinear interpolation method, however, exhibited comparatively poorer decoding performance. For the complete collimated dataset, the overall decoding errors obtained with the bicubic and nearest-neighbor interpolation methods across the 25×25 positions were 1.07 ± 0.45 mm and 1.00 ± 0.42 mm, respectively. The minimum positional errors of 0.37 mm and 0.36 mm were observed at the crystal center, while the maximum errors reached 2.51 mm and 2.24 mm at the corners.

The ML method demonstrated strong capability in handling noise and incomplete data, exhibiting excellent positioning performance in the LIOB-processed CsI: Tl crystal. Compared to CoG algorithm, the peak-to-valley ratio of the decoding map increased from 1.91 to at least 2.89 in the central crystal region, representing a 51.31% improvement. Notably, in the edge and corner regions—where the CoG method failed to provide clear pixel separation—the ML method, using both bicubic and nearest-neighbor interpolation, achieved distinct pixel discrimination. Two conclusions can be drawn regarding the optimization of the ML algorithm: (1) The nearest-neighbor interpolation method exhibited superior decoding performance compared with the bicubic method, as reflected by the improvement in overall positional accuracy from 1.07 ± 0.45 mm to 1.00 ± 0.42 mm across all 25×25 pixels. (2) Increasing the interpolation scale—and consequently the pixel resolution—further enhanced the decoding performance, as indicated by the rise in the peak-to-valley ratio in the central region from 2.89 to 3.17.

In the experiments, the collimated dataset was acquired using a ^{99m}Tc source with a photopeak energy of 140 keV, whereas the flood-irradiation experiment employed a ^{57}Co source with a photopeak energy of 122 keV. The flood-decoding maps indicated that variations in photon energy peaks had no significant influence on the applicability of the MDRF or the decoding performance of the ML method, as each converging pixel remained clearly distinguishable. This robustness can be attributed to the MDRF derivation, which is based on the relative energy contribution of each pixel to the total detected energy. In clinical SPECT applications, where different radionuclides with varying photopeak energies are often used, this characteristic ensures that the ML-based decoding approach remains reliable and energy-independent across multiple radiation sources.

In CoG algorithm, applying an energy threshold or selecting the channel with the highest energy can effectively suppress electronic noise and enhance decoding performance. A similar strategy was applied in the ML decoding; however, it did not produce any significant improvement in the decoding results. This finding indirectly confirms the intrinsic capability of the ML method to handle noise and incomplete data. Furthermore, an energy-iterative ML decoding approach based on equation (5) was implemented, which likewise did not yield any measurable enhancement in performance.

Several previous studies have attempted to optimize ML-based decoding performance through threshold analysis of likelihood probabilities. For example, Nicolas Gross-Weege *et al.* [44] investigated the effects of applying a likelihood-based filter on system sensitivity, energy resolution, and image

> REPLACE THIS LINE WITH YOUR MANUSCRIPT ID NUMBER (DOUBLE-CLICK HERE TO EDIT) <

quality. Similarly, Harrison H. Barrett *et al.* [45] reported that comparing the maximized likelihood to a threshold is an effective way to reject events depositing energy across multiple pixels while retaining both photoelectric and Compton interactions. In the present study, a similar threshold-comparison approach was employed. For instance, the decoding probabilities obtained using the bicubic interpolation method for the collimated dataset are illustrated in Fig. 16. However, this threshold-based analysis did not lead to a significant improvement in decoding performance, which may be attributed to the detector configuration and the specific radionuclide used, resulting in a relatively low occurrence of multiple-scatter events.

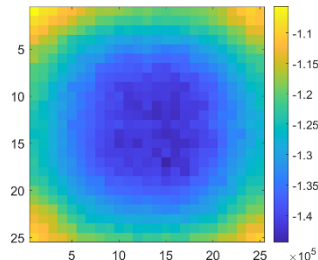


Fig. 16. Heat map of the average decoding probabilities obtained using the ML algorithm with bicubic interpolation for the collimated datasets.

In summary, this study demonstrated the feasibility of a laser-fabricated optical barrier technique for the design and fabrication of a converging-pixel CsI: Tl crystal. The results confirmed that the ML approach outperformed the CoG method, achieving clear and complete resolution of all crystal pixels. The successful fabrication and decoding of the proposed detector establish a solid foundation for the broader application of laser-processed scintillators in PET and SPECT systems, demonstrating their promising potential for high-resolution, high-sensitivity medical imaging. Future work will focus on employing artificial intelligence-based algorithms to further optimize the decoding process and to perform comparative analyses.

ACKNOWLEDGMENT

We acknowledge the initial involvement of Salar Sajedi in readout electronics.

REFERENCES

- [1] R. Van Patten, T. Greif, K. Britton, and G. Tremont, "Single-photon emission computed tomography (SPECT) perfusion and neuropsychological performance in mild cognitive impairment," *J. Clin. Exp. Neuropsychol.*, vol. 41, no. 5, pp. 530-543, Jul 2019, doi: 10.1080/13803395.2019.1586838.
- [2] U. Shrestha *et al.*, "Measurement of absolute myocardial blood flow in humans using dynamic cardiac SPECT and (99m)Tc-tetrofosmin: Method and validation," *J. Nucl. Cardiol.*, vol. 24, no. 1, pp. 268-277, Feb 2017, doi: 10.1007/s12350-015-0320-3.
- [3] Z. Keidar, O. Israel, and Y. Krausz, "SPECT/CT in tumor imaging: technical aspects and clinical applications," *Semin. Nucl. Med.*, vol. 33, no. 3, pp. 205-18, Jul 2003, doi: 10.1053/snuc.2003.127310.
- [4] J. M. Warwick, "Imaging of Brain Function Using SPECT," *Metab. Brain Dis.*, vol. 19, 2004.
- [5] A. Rahmim and H. Zaidi, "PET versus SPECT strengths, limitations and challenges," *Nucl. Med. Commun.*, vol. 29, no. 3, pp. 193-207, 2008.
- [6] G. Crisan, N. S. Moldovean-Cioroianu, D. G. Timaru, G. Andries, C. Cainap, and V. Chis, "Radiopharmaceuticals for PET and SPECT Imaging: A Literature Review over the Last Decade," *Int. J. Mol. Sci.*, vol. 23, no. 9, Apr 30 2022, doi: 10.3390/ijms23095023.
- [7] F. F. Alqahtani, "SPECT/CT and PET/CT, related radiopharmaceuticals, and areas of application and comparison," *Saudi. Pharm. J.*, vol. 31, no. 2, pp. 312-328, Feb 2023, doi: 10.1016/j.jpsps.2022.12.013.
- [8] D. Guberman, R. Paoletti, A. Rugliancich, C. Wunderlich, and A. Passeri, "Large-Area SiPM Pixels (LASiPs): A cost-effective solution towards compact large SPECT cameras," *Phys. Med.*, vol. 82, pp. 171-184, Feb 2021, doi: 10.1016/j.ejmp.2021.01.066.
- [9] S. R. Cherry, J. A. Sorenson, and M. E. Phelps, "Physics in nuclear medicine," 2003, ch. 14-The Gamma Camera: Performance Characteristics.
- [10] P. Ritt, "Recent Developments in SPECT/CT," *Semin. Nucl. Med.*, vol. 52, no. 3, pp. 276-285, May 2022, doi: 10.1053/j.semnuclmed.2022.01.004.
- [11] R. Massari and G. S. P. Mok, "New trends in single photon emission computed tomography (SPECT)," *Front. Med.*, vol. 10, p. 1349877, 2023, doi: 10.3389/fmed.2023.1349877.
- [12] X. Lai, L. Cai, J.-W. Tan, E. M. Zannoni, B. Odintsov, and L.-J. Meng, "Design, Performance Evaluation, and Modeling of an Ultrahigh Resolution Detector Dedicated for Simultaneous SPECT/MRI," *IEEE Trans. Radiat. Plasma Med. Sci.*, vol. 6, no. 1, pp. 42-50, 2022, doi: 10.1109/trpms.2021.3053592.
- [13] S. Xu, Z. Yan, and Q. Wei, "A Survey of Crystals for SPECT Imaging," *Crystals*, vol. 14, no. 12, 2024, doi: 10.3390/cryst14121039.
- [14] K. Iniewski, "CZT detector technology for medical imaging," *J. Instrum.*, vol. 9, no. 11, pp. C11001-C11001, 2014.
- [15] M. F. Santarelli *et al.*, "CZT Detectors-Based SPECT Imaging: How Detector and Collimator Arrangement Can Determine the Overall Performance of the Tomograph," *Electronics*, vol. 10, no. 18, 2021, doi: 10.3390/electronics10182230.
- [16] C. Szeles, "CdZnTe and CdTe materials for X-ray and gamma ray radiation detector applications," *Phys. Status Solidi B*, vol. 241, no. 3, pp. 783-790, 2004.
- [17] X. Yu *et al.*, "Requirements of Scintillation Crystals with the Development of PET Scanners," *Crystals*, vol. 12, no. 9, 2022, doi: 10.3390/cryst12091302.
- [18] S. Xie *et al.*, "Ultra-precise surface processing of LYSO scintillator crystals for Positron Emission

> REPLACE THIS LINE WITH YOUR MANUSCRIPT ID NUMBER (DOUBLE-CLICK HERE TO EDIT) <

[19] Tomography," *Appl. Surf. Sci.*, vol. 469, pp. 573-581, Mar 1 2019.

[20] J. Cabello, A. Etxeberste, G. Llosa, and S. I. Ziegler, "Simulation study of PET detector limitations using continuous crystals," *Phys. Med. Biol.*, vol. 60, no. 9, pp. 3673-94, May 7 2015, doi: 10.1088/0031-9155/60/9/3673.

[21] J. Cabello *et al.*, "High resolution detectors based on continuous crystals and SiPMs for small animal PET," *Nucl. Instrum. Methods Phys. Res. Sect. A*, vol. 718, pp. 148-150, 2013, doi: 10.1016/j.nima.2012.08.094.

[22] M. Kaul, S. Surti, R. Wiener, and J. S. Karp, "Thick continuous crystal design for PET," *IEEE NSS/MIC*, 2008.

[23] V. Nadig *et al.*, "ASICs in PET: what we have and what we need," *EJNMMI Phys.*, vol. 12, no. 1, p. 16, Feb 13 2025, doi: 10.1186/s40658-025-00717-8.

[24] P. Trigilio, P. Busca, R. Quaglia, M. Occhipinti, and C. Fiorini, "A SiPM-Readout ASIC for SPECT Applications," *IEEE Trans. Radiat. Plasma Med. Sci.*, vol. 2, no. 5, pp. 404-410, 2018, doi: 10.1109/trpms.2018.2856201.

[25] D. Meier, Sindre Mikkelsen, Jahanzad Talebi, Suleyman Azman, Gunnar Mæhlum, and B. E. Patt, "An ASIC for SiPM/MPPC Readout," presented at the IEEE NSS/MIC, 2010.

[26] A. Gonzalez-Montoro *et al.*, "Evolution of PET Detectors and Event Positioning Algorithms Using Monolithic Scintillation Crystals," *IEEE Trans. Radiat. Plasma Med. Sci.*, vol. 5, no. 3, pp. 282-305, 2021, doi: 10.1109/trpms.2021.3059181.

[27] L. Cong *et al.*, "Algorithms to reduce the edge effect and improve the flood histogram quality of a PET detector consisting of two pixelated crystal arrays," *Med. Phys.*, vol. 52, no. 2, pp. 856-866, Feb 2025, doi: 10.1002/mp.17484.

[28] Christoph W. Lerche, Torsten Solf, Peter Dueppenbecker, Benjamin Goldschmidt, P. K. Marsden, and V. Schulz., "Maximum Likelihood Based Positioning and Energy Correction for Pixelated Solid State PET Detectors," presented at the IEEE NSS/MIC, 2011.

[29] T. E. Peterson and L. R. Furenlid, "SPECT detectors: the Anger Camera and beyond," *Phys. Med. Biol.*, vol. 56, no. 17, pp. R145-82, Sep 7 2011, doi: 10.1088/0031-9155/56/17/R01.

[30] M. Streun, H. Nöldgen, G. Kemmerling, and S. van Waasen, "Position reconstruction in monolithic block detectors," presented at the IEEE NSS/MIC, 2012.

[31] X. Zhang *et al.*, "Performance of a SiPM based semi-monolithic scintillator PET detector," *Phys. Med. Biol.*, vol. 62, no. 19, pp. 7889-7904, Sep 21 2017, doi: 10.1088/1361-6560/aa898a.

[32] V. Dam *et al.*, "Improved nearest neighbor methods for gamma photon interaction position determination in monolithic scintillator PET detectors," *IEEE Trans. Nucl. Sci.*, vol. 58, no. 5, pp. 2139-2147, 2011.

[33] G. Borghi, V. Tabacchini, S. Seifert, and D. R. Schaart, "Experimental validation of an efficient fan-beam calibration procedure for K-nearest neighbor position estimation in monolithic scintillator detectors," *IEEE Trans. Nucl. Sci.*

[34] H. Arabi, A. AkhavanAllaf, A. Sanaat, I. Shiri, and H. Zaidi, "The promise of artificial intelligence and deep learning in PET and SPECT imaging," *Phys. Med.*, vol. 83, pp. 122-137, Mar 2021, doi: 10.1016/j.ejmp.2021.03.008.

[35] V. Balaji, T. A. Song, M. Malekzadeh, P. Heidari, and J. Dutta, "Artificial Intelligence for PET and SPECT Image Enhancement," *J. Nucl. Med.*, vol. 65, no. 1, pp. 4-12, Jan 2 2024, doi: 10.2967/jnumed.122.265000.

[36] P. Bruyndonckx *et al.*, "Neural network-based position estimators for PET detectors using monolithic LSO blocks," *IEEE Trans. Nucl. Sci.*, vol. 51, no. 5, pp. 2520-2525, 2004, doi: 10.1109/tns.2004.835782.

[37] *Performance Study of Neural Network Position Estimators for the Monolithic Scintillator PET detector Modules.* (2010).

[38] S. S. Gambhir *et al.*, "A novel high-sensitivity rapid-acquisition single-photon cardiac imaging camera," *J. Nucl. Med.*, vol. 50, no. 4, pp. 635-43, Apr 2009, doi: 10.2967/jnumed.108.060020.

[39] T. Funk, P. Després, W. C. Barber, K. S. Shah, and B. H. Hasegawa, "A multipinhole small animal SPECT system with submillimeter spatial resolution," *Med. Phys.*, vol. 33, no. 5, pp. 1259-1268, 2006.

[40] F. Caobelli *et al.*, "IQ SPECT allows a significant reduction in administered dose and acquisition time for myocardial perfusion imaging: evidence from a phantom study," *J. Nucl. Med.*, vol. 55, no. 12, pp. 2064-70, Dec 2014, doi: 10.2967/jnumed.114.143560.

[41] M. Havel, M. Kolacek, M. Kaminek, V. Dedek, O. Kraft, and P. Sirucek, "Myocardial perfusion imaging parameters: IQ-SPECT and conventional SPET system comparison," *Hell. J. Nucl. Med.*, vol. 17, pp. 200-203, 2014.

[42] M. U. Zaman, I. Hashmi, and N. Fatima, "Recent developments and future prospects of SPECT myocardial perfusion imaging," *Ann. Nucl. Med.*, vol. 24, no. 8, pp. 565-9, Oct 2010, doi: 10.1007/s12149-010-0400-z.

[43] H. Sabet, L. Blackberg, D. Uzun-Ozsahin, and G. El-Fakhri, "Novel laser-processed CsI:Tl detector for SPECT," *Med. Phys.*, vol. 43, no. 5, p. 2630, May 2016, doi: 10.1118/1.4947294.

[44] X. Zhang *et al.*, "Design study of a PET detector with 0.5 mm crystal pitch for high-resolution preclinical imaging," *Phys. Med. Biol.*, vol. 66, no. 13, p. p.135013, Jul 1 2021, doi: 10.1088/1361-6560/ac0b82.

[45] N. Gross-Weege, D. Schug, P. Hallen, and V. Schulz, "Maximum likelihood positioning algorithm for high-

> REPLACE THIS LINE WITH YOUR MANUSCRIPT ID NUMBER (DOUBLE-CLICK HERE TO EDIT) <

resolution PET scanners," *Med. Phys.*, vol. 43, no. 6, pp. 3049-3061, Jun 2016, doi: 10.1118/1.4950719.

[45] H. H. Barrett, W. C. J. Hunter, B. W. Miller, S. K. Moore, Y. Chen, and L. R. Furenlid, "Maximum-Likelihood Methods for Processing Signals From Gamma-Ray Detectors," *IEEE Trans. Nucl. Sci.*, vol. 56, no. 3, pp. 725-735, 2009, doi: 10.1109/tns.2009.2015308.